arXiv:1412.0476v1 [astro-ph.GA] 1 Dec 2014

Tracing H_2 column density with atomic carbon (C I) and CO isotopologs

N. Lo

Departamento de Astronomía, Universidad de Chile, Camino El Observatorio 1515, Las Condes, Santiago, Casilla 36-D, Chile

M. R. Cunningham and P. A. Jones

School of Physics, University of New South Wales, Sydney, NSW 2052, Australia

L. Bronfman

Departamento de Astronomía, Universidad de Chile, Camino El Observatorio 1515, Las Condes, Santiago, Casilla 36-D, Chile

P. C. Cortes

Joint ALMA Observatory, Santiago, Chile

R. Simon

Physikalisches Institut, Universität zu Köln, Zülpicher Straße 77, 50937 Köln, Germany

V. Lowe

School of Physics, University of New South Wales, Sydney, NSW 2052, Australia

Australia Telescope National Facility, CSIRO Astronomy and Space Science, PO Box 76, Epping, NSW 1710, Australia

L. Fissel and G. Novak

Northwestern University, Center for Interdisciplinary Exploration and Research in Astrophysics (CIERA) and Department of Physics & Astronomy, 2145 Sheridan Road, Evanston, IL 60208, USA

Received _____; accepted _____

ABSTRACT

We present first results of neutral carbon ([C I] $^3P_1 - ^3P_0$ at 492 GHz) and carbon monoxide (^{13}CO, J = 1 - 0) mapping in the Vela Molecular Ridge cloud C (VMR-C) and G333 giant molecular cloud complexes with the NANTEN2 and Mopra telescopes. For the four regions mapped in this work, we find that [C I] has very similar spectral emission profiles to ^{13}CO, with comparable line widths. We find that [C I] has opacity of 0.1 - 1.3 across the mapped region while the [C I]/^{13}CO peak brightness temperature ratio is between 0.2 to 0.8. The [C I] column density is an order of magnitude lower than that of ^{13}CO. The H_2 column density derived from [C I] is comparable to values obtained from ^{12}CO. Our maps show C I is preferentially detected in gas with low temperatures (below 20 K), which possibly explains the comparable H_2 column density calculated from both tracers (both C I and ^{12}CO under estimate column density), as a significant amount of the C I in the warmer gas is likely in the higher energy state transition ([C I] $^3P_2 - ^3P_1$ at 810 GHz), and thus it is likely that observations of both the above [C I] transitions are needed in order to recover the total H_2 column density.

Subject headings: ISM: atoms — ISM: molecules — ISM: clouds — stars: individual (RCW36, IRAS16172-5028, IRAS16177-5018, IRAS16164-5046) — stars: formation

1. Introduction

Carbon monoxide (CO) is often used as a tracer of H_2 density in molecular clouds, as it is abundant and easy to observe. However, it is known to be unreliable as it is optically thick in star forming regions (e.g. Shetty et al. 2011). With a new generation of telescopes capable of mapping at sub-millimeter wavelengths, there is a revival of interest in utilizing neutral atomic carbon as a tracer of molecular cloud column density, both observationally and in numerical simulations (see e.g. Shimajiri et al. 2013; Offner et al. 2014; Glover et al. 2014). One of the perceived advantages of atomic carbon (C I) over CO is that it continues to exist in regions of low dust extinction and strong radiation (commonly found in star forming regions), where CO suffers from photodissociation and turns into neutral carbon and oxygen. Here we investigate the effect that density and temperature have on H_2 column density calculated from [C I] and how it compares to that calculated from the CO isotopologues.

Of the four sources mapped here (see Table 1), three are in the G333 GMC, located at a distance of 3.6 kpc, while NE-RCW36 is north-east of the RCW36 H II region in the Vela Molecular Ridge cloud C (VMR-C) at a distance of 700 pc. Both the G333 and VMR-C clouds have been extensively mapped at various wavelengths, including IR (Spitzer GLIMPSE and MIPSGAL, BLAST, Herschel), millimeter dust, and molecular lines (e.g. Yamaguchi et al. 1999; Mookerjea et al. 2004; Wong et al. 2008; Lo et al. 2009; Netterfield et al. 2009). From 1.2 mm dust continuum observations, the sources (clumps) in G333 have masses of $\sim 10^3$ $M_\odot$ (Mookerjea et al. 2004), while the clumps in NE-RCW36 have an order of magnitude lower mass of ~ 70 $M_\odot$ (Netterfield et al. 2009). Over the last two years, we have started a program to map these two clouds in atomic carbon emission, with the NANTEN2 Telescope in Chile. We aim to investigate the distribution of C I in comparison to not only the CO isotopologues, but also various other chemical species such

as N_2H^+, HNC, CS, and other dense gas tracers between 86 and 99 GHz.

We are currently completing the mapping of C I in G333 and the VMR-C, and here present our first result from the four mapped regions, focusing on the comparison between C I and CO isotopologues. The selected regions are all associated with embedded stellar clusters and H II regions (see Table 1).

2. Observations and data reduction

The atomic carbon ([C I] ($^3P_1 - ^3P_0$) at 492.16 GHz, hereafter simply referred to as [C I]) observations presented in this paper were carried out in 2013 with the NANTEN2 Telescope[1] at Pampa la Bola, Chile. The maps were collected with the 2×8 pixel array KOSMA SMART receiver and a eXtended bandwidth Fast Fourier Transfer Spectrometer (XFFTS) as backend, 2.5 GHz bandwidth and 32768 channels. At 465 GHz it has a full width to half-maximum (FWHM) beam size of ~ 37 arcseconds. Data were reduced with CLASS (GILDAS package), and have velocity resolution of 0.2 $\mathrm{km\,s^{-1}}$.

The CO, ^{13}CO and C^{18}O maps were collected with the Mopra Telescope throughout 2005 to 2007 for G333, 2012 and 2014 for VMR-C (for details see Bains et al. 2006; Wong et al. 2008; Lo et al. 2009). At 3 mm wavelengths the Mopra telescope has a FWHM beam size of ∼36 arcseconds and velocity resolution of ~ 0.1 $\mathrm{km\,s^{-1}}$ $\mathrm{channel^{-1}}$ at 100 GHz (Ladd et al. 2005). Data were reduced using the Livedata and Gridzilla packages from the CSIRO/CASS. The Mopra data are gridded to the same spacing as the NANTEN2 [C I] data, which equates to 0.13 pc for RCW36 and 0.64 pc for the three G333 sources.

[1]http://www.astro.uni-koeln.de/nanten2/

3. Results

3.1. Spatial and velocity distributions

Integrated emission maps of ^{13}CO (contours) overlaid on [C I] (color) of the four sources are shown in Figure 1. Integrated velocity ranges are -70 to -52 km s^{-1} for IRAS16164–5046, -65 to -33 km s^{-1} for IRAS16172–5028 and IRAS16177–5018, and 2 to 12 km s^{-1} for NE-RCW36. There are two distinct velocity components in IRAS16164–5046 (Figure 2 spectra), -57 km s^{-1} is the main component while the -48 km s^{-1} component is due to a source south-east of IRAS16164–5046 and is outside the presented map. Hence the intensity map and calculations follow are based on emission integrated over the -57 km s^{-1} velocity component for this source.

In general the bulk of [C I] emission for the three G333 sources has a similar distribution to the ^{13}CO emission, with its peak integrated emission also coinciding well with ^{13}CO, such as the ring-structure seen in IRAS16177–5018 (Figure 1 bottom left). In contrast for NE-RCW36 (Figure 1 bottom right) there are two [C I] peaks, the north-east peak (RA $= 9^{\rm h}59^{\rm m}32^{\rm s}$, Dec $= -43^{\rm d}43^{\rm m}50^{\rm s}$) does not have any corresponding ^{13}CO emission peak, and the south-west one (RA $= 9^{\rm h}59^{\rm m}23^{\rm s}$, Dec $= -43^{\rm d}45^{\rm m}00^{\rm s}$) is offset from the ^{13}CO clump (contours).

To show the velocity structure of these regions, position-velocity (PV) diagrams of [C I] (grey scale) and ^{13}CO (contours) are plotted in Figure 2 (top row), with line profiles of [C I] and ^{13}CO averaged over the region in the integrated emission maps (Figure 1 bottom four). [C I] and ^{13}CO have similar velocity structure, in the form of centroid velocity, line widths, line wings/shoulders due to outflows and infall, as show in the Gaussian fitted parameters of the spectra (Table 1). As mentioned previously, the -48 km s^{-1} component of IRAS16164–5046 is due to a different source outside the presented map; here the PV

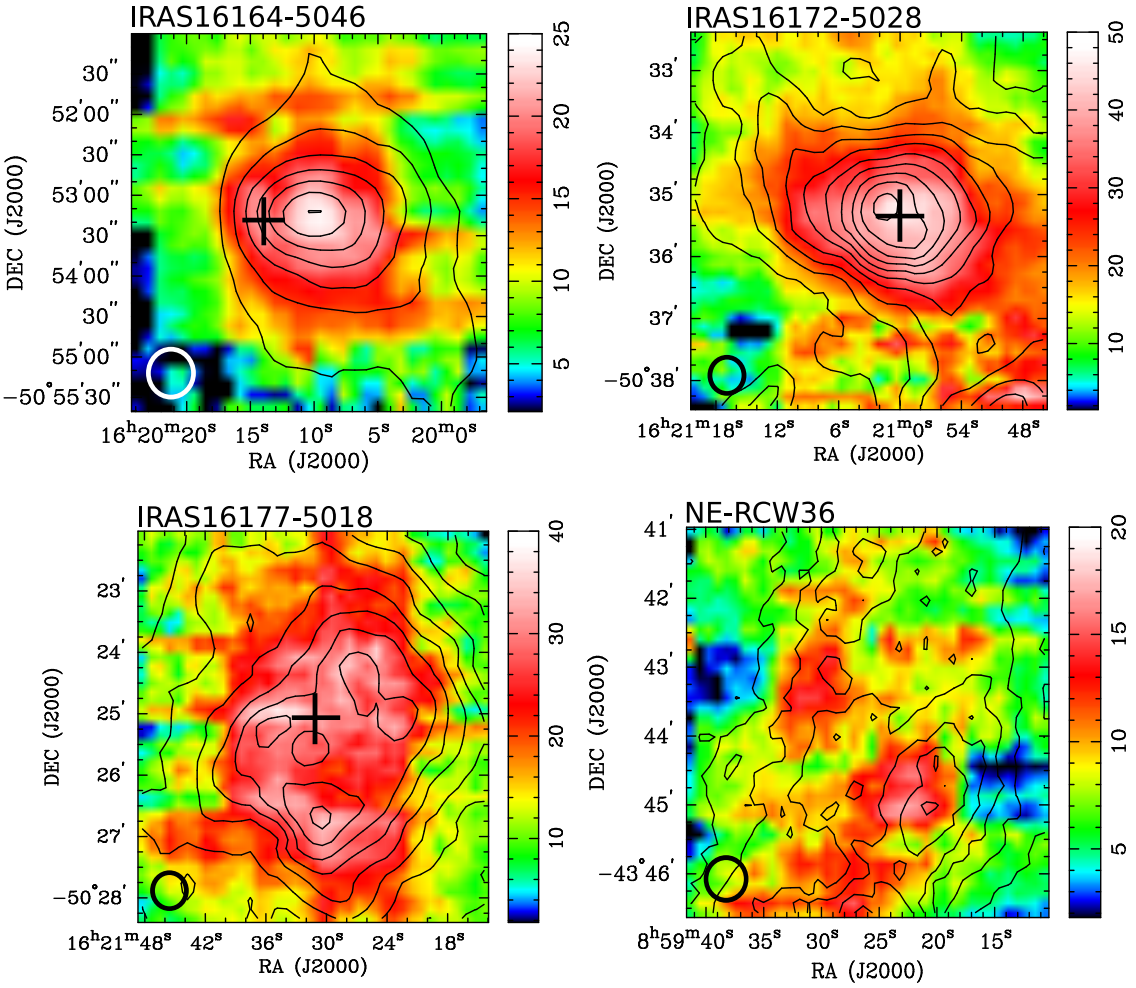

Fig. 1.— Integrated emission maps of ^{13}CO (contours) overlaid on [C I] of the four sources. The ^{13}CO contour levels start at 30 per cent of the peak integrated emission, with increments of 10σ for NE-RCW36, and 20σ for the other three sources. ^{13}CO peak integrated emission are 131, 189, 164 and 28 K km s^{-1} for IRAS16164–5046, IRAS16172–5028, IRAS16177–5018 and NE-RCW36 respectively. 1σ level of ^{13}CO integrated emission maps are 0.7 K km s^{-1} for IRAS16164–5046, IRAS16172–5028 and IRAS16177–5018, 0.3 K km s^{-1} for NE-RCW36, 3σ level are outside the presented ^{13}CO maps. Color scales are clipped at 3σ level, where 1σ is 0.7 K km s^{-1} for IRAS16164–5046 and IRAS16172-5028, 0.6 K km s^{-1} for IRAS16177-5018 and NE-RCW36. Beam sizes are marked by circles. The crosses mark the location of the *IRAS* sources, except RCW36 which is outside the map.

diagram shows that this emission is detached from the main source. NE-RCW36 PV diagram shows two separate velocity components, 4 and 7 $\mathrm{km\,s^{-1}}$, which are also spatially separated. Since the column density calculation in this work is per spatial pixel, any spatially separable velocity structure does not affect the derivation of column density.

^{13}CO generally appears to be more extensive than [C I] as shown in Figure 1. However, we have determined that this is due the greater prevalence of artifacts in [C I] maps, compared with those of ^{13}CO maps. The noise in both ^{13}CO and [C I] maps is non-Gaussian, and is influenced in particular by fluctuations in weather at the times maps were taken. For [C I] at the higher frequency of 492 GHz, maps are more affected by poor weather than ^{13}CO transition at 110 GHz. As the artifacts/noise are non-Gaussian, it has not been possible to determine a specific contour level of ^{13}CO below which [C I] is no longer detected.

3.2. Column densities

The column density maps presented in this work is derived per spatial pixel, utilizing the integrated intensity maps in Section 3.1. H_2 column density is obtained from the optically thick ^{12}CO, C I, and ^{13}CO column densities are corrected for opacity at each spatial pixel position.

For H_2 column density, we utilize the empirical relation between H_2 and ^{12}CO for Galactic molecular clouds (Shetty et al. 2011),

$$N_{\mathrm{H_2}} = 2 \times 10^{20} \int T_{\mathrm{MB}}(\mathrm{CO, J = 1 \rightarrow 0}) dV \,. \quad (1)$$

We follow the column density calculation outlined in Oka et al. (2001) for C I, which

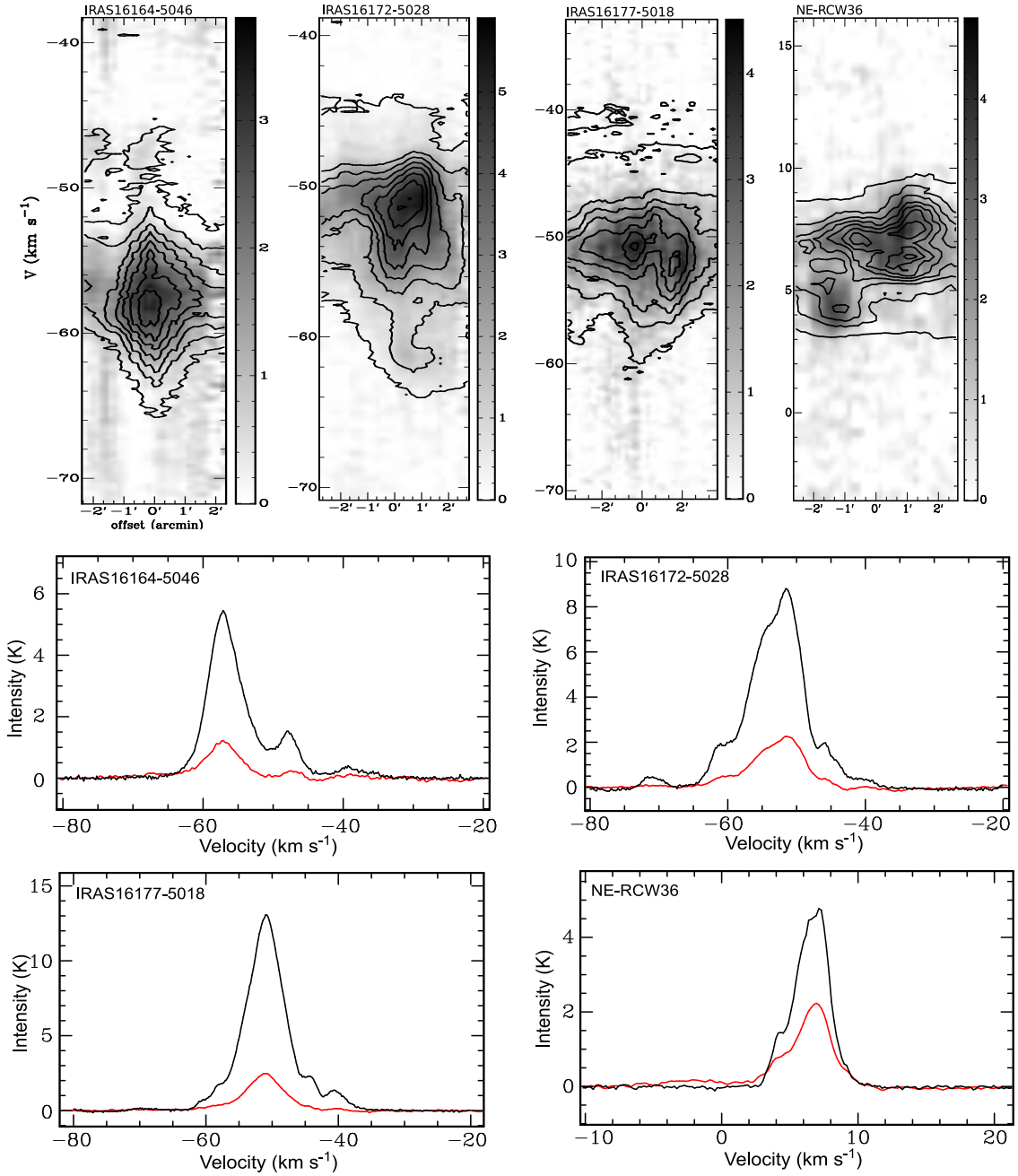

Fig. 2.— (*Top row*) [C I] and ^{13}CO (contours) position-velocity (PV). The contour levels start at 5σ noise level with increment of 10σ, where 1σ is 0.2 K for IRAS16164–5046, 0.3 K for IRAS16172–5028 and IRAS16177–5018, and 0.1 K for NE-RCW36. PV cuts across each of the sources from NE to SW. (*Line profiles*) Averaged [C I] (red) and ^{13}CO (black) spectra over the area shown in Figure 1.

we repeat briefly here,

$$N_{\rm CI} = 1.98 \times 10^{15} \int T_{\rm MB} dV\, Q(T_{\rm ex}) e^{E_1/(kT_{\rm ex})} \times \left[1 - \frac{J_\nu(T_{\rm BB})}{J_\nu(T_{\rm ex})}\right]^{-1} \frac{\tau_{\rm CI}}{1 - e^{-\tau_{\rm CI}}}, \tag{2}$$

where $\int T_{\rm MB} dV$ is the integrated emission of [C I], $Q(T_{\rm ex})$ is the partition function,

$$Q(T_{\rm ex}) = 1 + 3{\rm e}^{E_1/(kT_{\rm ex})} + 5{\rm e}^{E_2/(kT_{\rm ex})}\,, \tag{3}$$

with energy levels of $E_1/k = 23.6$ K and $E_2/k = 62.5$ K, $J_\nu(T_{\rm BB})$ and $J_\nu(T_{\rm ex})$ are the radiation temperature of cosmic background radiation ($T_{\rm BB} = 2.7$ K) and excitation temperature ($T_{\rm ex}$) respectively, and $\tau_{\rm CI}$ is the opacity,

$$\tau_{\rm CI} = -\ln\left\{1 - \frac{T_{\rm MB}}{\eta_f \left[J_\nu(T_{\rm ex}) - J_\nu(T_{\rm BB})\right]}\right\}\,, \tag{4}$$

here we assume the beam filling factor $\eta_f = 1$. Assuming C I has the same excitation temperature as the optically thick ^{12}CO at each of the spatial pixels, which is derived from the peak brightness temperature of ^{12}CO (Glover et al. 2014). We found the opacity of C I is between 0.1 to 1.3 across the maps. The total column density of C I is between $(0.1 - 8.4) \times 10^{17}$ cm^{-2}, where IRAS16172–5028 has the highest peak column density of 8.4×10^{17} cm^{-2}, and NE-RCW36 has the lowest peak column density of 3.3×10^{17} cm^{-2}.

For ^{13}CO column density, we corrected ^{13}CO opacity by assuming that C^{18}O is optically thin, and taking an isotopologue ratio of $\tau_{\rm 13CO} = 7.4\tau_{\rm C18O}$ for the three sources in G333 GMC (Wong et al. 2008), and 5.5 for NE-RCW36. The opacity is then obtained by solving the brightness temperature-opacity relation,

$$\frac{T_{\rm 13CO}}{T_{\rm C18O}} = \frac{1 - e^{-\tau_{\rm 13CO}}}{1 - e^{-\tau_{\rm C18O}}}. \tag{5}$$

Similar to C I, we assume ^{13}CO has the same excitation temperature as ^{12}CO, the total column density of ^{13}CO is then,

$$N = \frac{8k\pi\nu^2}{hc^3 g_{\rm u} A_{\rm ul}} \frac{\tau}{1 - e^{-\tau}} e^{-E_u/(kT_{\rm ex})} Q(T_{\rm ex}) \int T_{\rm b} dV\,, \tag{6}$$

where $\int T_{\rm b} dV$ is the integrated emission of ^{13}CO, upper energy level of $E_u/k = 5.3$ K, $A_{\rm ul}$ is the Einstein A coefficient in s^{-1}, transition frequency ν in Hz, the degeneracy g_u, and $Q(T_{\rm ex})$ is the partition function (Garden et al. 1991). We found the opacity of ^{13}CO to be between 0.1 and 5.3, and column density in the range of $(0.1 - 100) \times 10^{17}$ cm^{-2}. IRAS16172–5028 and IRAS16177–5018 have the highest peak column density ($\sim 10^{19}$ cm^{-2}), while similar to C I, NE-RCW36 has the lowest peak column density of 1.1×10^{18} cm^{-2}.

Simulation and modeling on how well C I traces molecular clouds suggest the $X_{\rm CI} - factor$ has a value of 1.1×10^{21} cm^{-2} K^{-1} km^{-1} s, an analogue to the widely used $X_{\rm CO} - factor$ that connects integrated ^{12}CO emission to H_2 column density (e.g. Offner et al. 2014; Glover et al. 2014). We apply this value to the integrated emission maps of [C I] to derive H_2 column density ($N_{\rm H2-CI}$) and compare this to the H_2 column density maps we obtained from ^{12}CO maps ($N_{\rm H2-CO}$). We note that the conversion factor is obtained from simulation and may not be fully applicable to the observed region here, due to variables such as local abundance, chemical and physical conditions. We found $N_{\rm H2-CI}$ traces 80 to 100 per cent of $N_{\rm H2-CO}$ for regions where ^{13}CO column density is between ~ 5 to 7×10^{18} cm^{-2} and C I column density is between ~ 4 to 8×10^{17} cm^{-2} for the three G333 *IRAS* sources, for NE-RCW36, the region is at $\sim 1 \times 10^{17}$ cm^{-2} for ^{13}CO and ~ 2 to 3×10^{17} cm^{-2} for C I. A summary of the derived physical properties are listed in Table 1.

4. Discussion

Recent C I mapping of the northern part of Orion-A GMC by Shimajiri et al. (2013) found a opacity of 0.1 - 0.75, similar to what we find (0.1 - 0.8) for three of our sources, with the exception of IRAS16164–5046 which reaches as high as 1.3 in optical depth at the [C I] emission peak. The highest C I column density in this work is of order of $\sim 10^{17}$ cm^{-2}, which is an order of magnitude lower than the peak value $\sim 10^{18}$ cm^{-2} found in Orion-A.

Table 1: Observational and physical parameters of the sources.

	IRAS16164–5046[a]	IRAS16172–5028[b]	IRAS16177–5018[c]	NE-RCW36[d]
Pointing center[e] (α, δ)	16 22.17, -50 06.1	16 21.06, -50 35.38	16 21.54, -50 25.33	08 59.43, -43 43.87
Parent Complex	G333	G333	G333	VMR-C
Distance	3.6 kpc[f]	3.6 kpc[f]	3.6 kpc[f]	0.7 kpc[g]
rms chan^{-1}	0.4/0.3 K	0.3/0.3 K	0.3/0.3 K	0.3/0.2 K
(NANTEN2/Mopra)				
$V_{\rm CI}$ (km s^{-1})[h]	−47, −57	−45, −51, −54, −61	−45, −51, −58	4.2, 7.0
$V_{\rm 13CO}$ (km s^{-1})[h]	−48, −57	−45, −51, −54, −61	−40, −43, −50, −56	4.2, 7.0
$\Delta V_{\rm CI}$ (km s^{-1})[h]	2.5, 5.9	1.7, 5.6, 6.2, 4.4	6.7, 6.0, 6.5	2.5, 2.7
$\Delta V_{\rm 13CO}$ (km s^{-1})[h]	5.9, 5.6	2.8, 4.2, 6.2, 3.1	4.2, 3.1, 6.0, 6.8	1.5, 2.6
$\tau_{\rm CI}$[j]	0.2 - 1.3 (0.5)	0.2 - 0.8 (0.3)	0.1 - 0.6 (0.3)	0.1 - 0.8 (0.3)
$\tau_{\rm 13CO}$[j]	0.9 - 5.3 (2.8)	0.1 - 5.3 (2.2)	0.1 - 4.3 (2.2)	0.04 - 3.0 (0.5)
$N_{\rm CI}$ ($\times 10^{17}$ cm^{-2})[j]	0.2 - 7 (2.2)	0.9 - 8 (2.9)	0.1 - 6 (2.6)	0.1 - 3 (1.3)
$N_{\rm 13CO}$ ($\times 10^{17}$ cm^{-2})[j]	3 - 59 (9.6)	0.3 - 99 (19)	0.5 - 100 (28)	0.1 - 11 (0.8)
$T_{\rm ex}$ (K)[j]	8 - 16 (12)	14 - 29 (19)[j]	17 - 29 (21)	12 - 34 (19)
$N_{\rm H2-CO}$ ($\times 10^{22}$ cm^{-2})[k]	0.5 - 2.2 (1.9)	2.4 - 6.6 (3.7)	2.8 - 5.6 (3.9)	0.7 - 2.1 (1.3)
$N_{\rm H2-CI}$ ($\times 10^{22}$ cm^{-2})[k]	0.3 - 2.6 (0.8)	1.1 - 5.1 (1.8)	0.8 - 4.1 (1.6)	0.3 - 1.9 (0.9)

[a]**IRAS16164–5046**: One of the most luminous far-infrared (FIR) sources in the Galaxy (Becklin et al. 1973); associated with the H II region G333.6-0.22, H_2O and OH masers (Batchelor et al. 1980; Caswell 1998); harbours a young OB cluster (e.g. Fujiyoshi et al. 2006; Grave et al. 2014). [b]**IRAS16172-5028**: Strongest source of SiO emission in G333 (Lo et al. 2007). Associated with H II region G333.1-0.4, contains an embedded OB star cluster in very early evolutionary stages (Figueredo et al. 2005), and H_2O, OH and CH_3OH masers (Breen et al. 2007; Caswell 1998; Caswell et al. 1995). [c]**IRAS16177–5018**: Part of the H II region RCW106, contains the ultrahot star IRS1, likely an O3 I supergiant (Roman-Lopes et al. 2009). [d]**NE-RCW36**: Associated with the RCW36 H II region, which contains a cluster of several hundred stars with the most massive star being a type O8 or O9 (see Minier et al. 2013, and references therein). [e]The coordinates denote pointing centers for the maps (J2000). [f]Lockman (1979). [g]Murphy & May (1991). [h]Velocity component (V) and line width (ΔV) obtained from Gaussian fits to the spectra in Figure 2. [j]Opacity (τ), column density (N) of the C I and ^{13}CO maps, excitation temperature ($T_{\rm ex}$) derived from peak ^{12}CO emission, [k]H_2 column density derived from ^{12}CO ($N_{\rm H2-CO}$) and C I ($N_{\rm H2-CI}$). Note the ranges for j and k indicate the highest and lowest values across the maps of each of the sources (not per pixel), and median values are in brackets.

However, this could be due to effects such as resolution (i.e. beam filling factor less than 1). In fact, from modeling with the radiative transfer code RADEX (Van der Tak et al. 2007) for gas temperature shows 10^{18} cm^{-2} fits our sources better (discussion later on).

We also find that the C I column density peak is offset from the peak H_2 column density when the excitation temperature (both quantities derived from the peak ^{12}CO emission, Section 3.2) at the H_2 peak column density exceeds 25 K (Figure 3). This is unlikely to be due to the optical thickness of ^{12}CO 'shifting' the apparent peak position, as from a cross check with the dust cores from ATLASGAL (Csengeri et al. 2014) and BLAST (Netterfield et al. 2009) data, their positions coincide well with the ^{12}CO peaks and thus the H_2 column density peaks, except for source IRAS16177–5018, in which ^{12}CO is blended over various dust cores. In fact, at the peak C I column density position, $T_{\rm ex}$ is within 15 to 20 K. The only source (IRAS16164–5046) that has both the C I and H_2 column density peaks coincide has an excitation temperature of $\sim$ 15 K at this position. Furthermore, if we double the excitation temperature ($>$ 30 K) in C I column density calculations, it yields a lower column density at the C I peak position. Modeling of C I by Glover et al. (2014) shows around 80 per cent of C I is found in regions with temperature below 30 K, and from our observations, we also find C I is concentrated at places with lower excitation temperature (15 to 20 K). Depending on optical thickness, excitation temperature does not necessary equal gas kinetic temperature, and in the low opacity case, molecules are generally sub-thermally excited which makes the excitation temperature lower than kinetic temperature, so in either case, C I is found mainly in low temperature gas. One possible explanation for this is that the C I data presented here is from the observations of lower fine structure transition at 492 GHz with an energy level of 23 K. As the gas temperature rises, more of the neutral carbon atoms populate the higher transition level at 810 GHz with energy level of 62 K. To check whether this explanation is possible, we utilize the radiative transfer code RADEX by inputting gas temperatures in the range of 15 to 40 K. We find

that as temperature rises, the intensity (population) of the 810 GHz transition increases from 2.8 to 20 K. Furthermore, the H_2 column density we obtained with C I is comparable to H_2 column density derived from ^{12}CO, in which ^{12}CO is an unreliable tracer at high density as it becomes optically thick (e.g. Shetty et al. 2011), and thus under estimates the column density. Despite that, the comparable H_2 column density is suggesting that a portion of the neutral carbon atoms in the $^3P_1 - ^3P_0$ state appear to be missing. If this is the case, and if a substantial amount of atomic carbon is in an energy state above the ground state, we should see a position offset of the 810 GHz [C I] transition for the sources here, and follow up observations in the future will further investigate this. More importantly, observations of both [C I] transitions maybe necessary to recover the total C I gas.

One possible uncertainty in our column density calculation comes from the velocity range in the integrated intensity maps. As shown in Section 3.1 these sources are not quiescent gases, they are turbulent with outflows (line wings). In order to access the effect of integrating over different gas components on column density derivation, two sets of velocity range are used: (1) integration over a velocity range that includes line wings/shoulders, (2) integration over the line width of the main core velocity component. In method (1), the H_2 column density derived from [C I] is comparable to those derived from ^{12}CO (Table 1). With method (2), H_2 column density obtained from [C I] is approximately 10 to 30 per cent higher than those from ^{12}CO, but still within an order of magnitude. However, by integrating over the line width only can be problematic with ^{12}CO, as it is self-absorbed at the core velocity component, and the application of $X - factor$ requires ^{12}CO being optically thick and an integration over the emission range. Given the H_2 column density derived from ^{12}CO and [C I] in both methods are comparable and within the same order of magnitude, the choice of velocity range does not alter the conclusion in this work.

Another uncertainty in deriving H_2 column density is the value of $X_{\rm CI} - factor$, unlike

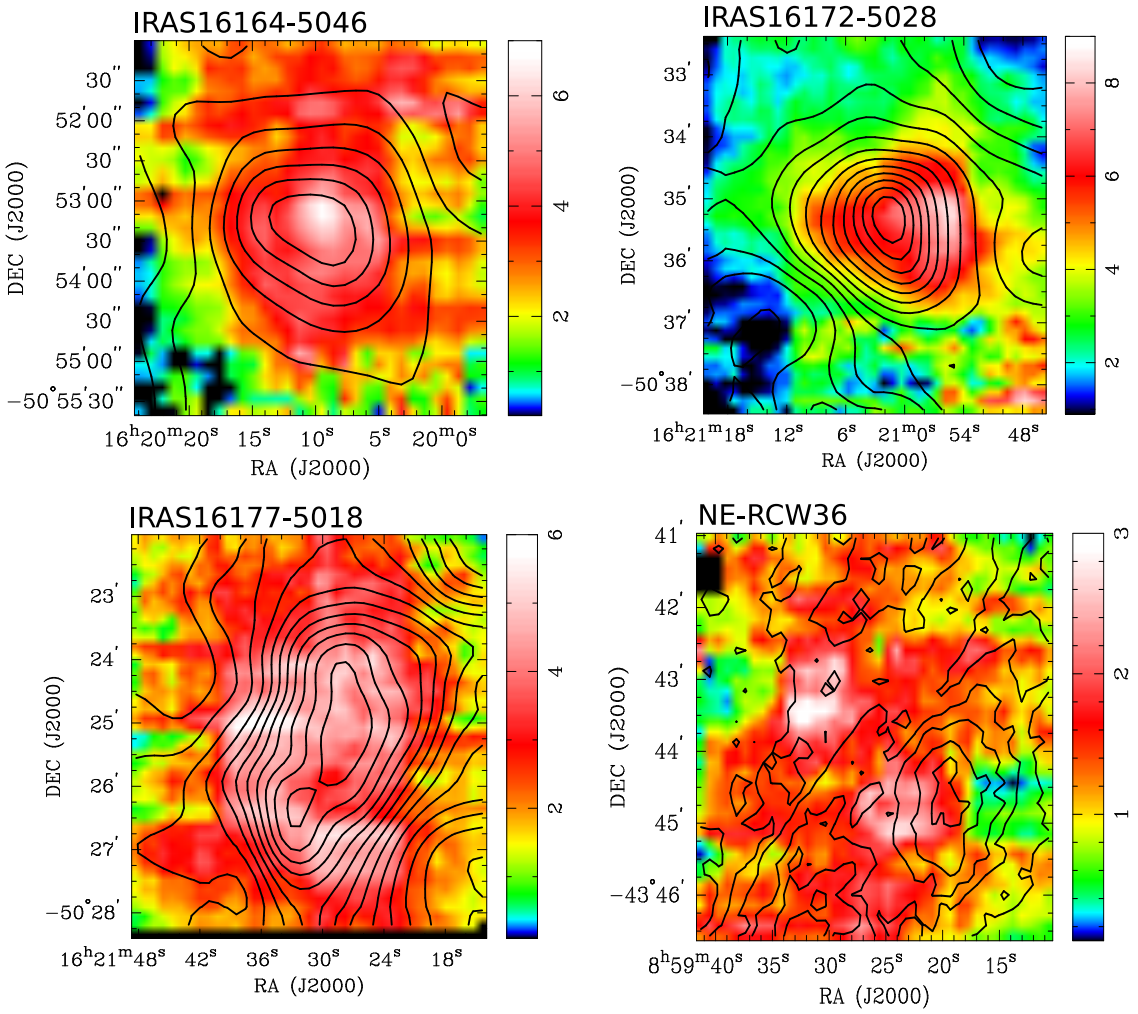

Fig. 3.— H_2 column density map (contours) overlaid on C I column density map (color) of the four sources. The column density maps are at scale of 10^{21} cm^{-2} and 10^{17} cm^{-2} for H_2 and C I. The H_2 contour levels start at 40 per cent of peak column density (Table 1), except for IRAS16177–5018 which start at 50 per cent, the lowest visible contour level in the presented map. Contour steps are at 20σ, where 1σ is 1×10^{20} cm^{-2} for IRAS16164–5046, IRAS16177–5018 and NE-RCW36, and 1.5×10^{20} for IRAS16172-5028.

CO, the relationship between [C I] intensity and H_2 column density is not well studied. The value we used in this work is from simulation studies (Offner et al. 2014; Glover et al. 2014), not specifically calibrated for the presented regions. The simulations do not take into account active star formation, where strong UV radiation increases the abundance of C I, and thus, altering the value of $X_{\rm CI} - factor$. There is no observational/simulation study on $X_{\rm CI} - factor$ among active star forming regions (at the time of this work), but if star formation raises the abundance of C I, then the $X_{\rm CI} - factor$ would be higher in these cases, and thus increases the derived H_2 column density. We are in the process of completing the C I mapping, along with various molecular lines at 3 mm wavelengths, we can calibrate the $X - factor$ of C I and other molecules (e.g. HCO^+, CS, HCN) by comparing the H_2 density estimated from SED fits of continuum emissions.

5. Conclusion

We present the first results of C I mapping of VMR-C and G333 GMCs, comparing the column density of H_2 derived from both C I and CO isotopologues. The [C I] emission profile is similar to ^{13}CO with comparable line widths. We found C I has opacity between 0.1 to 1.3, column density of $(0.1 - 8) \times 10^{17}$ cm^{-2}, an order of magnitude lower than ^{13}CO column density. Utilizing the $X_{\rm CI} - factor$ we found an H_2 column density of order $\sim 10^{22}$ cm^{-2}, which is within the same order of magnitude of H_2 column density derived from ^{12}CO, and near 100 per cent at [C I] peak emission location. [C I] emission tends to peak at regions with low gas temperature (< 20 K), and it yields the same H_2 column density as those derived from ^{12}CO at this temperature range. This could be due to part of the carbon atoms are in a higher excitation state, further mapping of C I transition at 810 GHz will help confirm this.

Our results suggest if the gas is warm (above 25 K), it is recommended to observe both

of the [C I] transitions for a more accurate determination of H_2 column density. C I has the advantage of low opacity compared to ^{12}CO, while in low density and low extinction regions CO is dissociated into neutral carbon and oxygen, making C I a better tracer in these cases. However, in regions of dense gas where local abundance of ^{13}CO is known, ^{13}CO may be a better choice for probing H_2 column density, as it is easily observed due to the lower frequency of its emission lines.

NL's postdoctoral fellowship is supported by CONICYT/FONDECYT postdoctorado, under project no. 3130540. LB acknowledges support by CONICYT Project PFB06. NANTEN2 Observatory is a collaboration between Nagoya University, Osaka University, KOSMA, Universität zu Köln, Argelander-Institet Universität Bonn, Seoul National University, ETH Zürich, University of New South Wales and Universidad de Chile. Mopra Telescope is part of the Australia Telescope and was funded by the Commonwealth of Australia for operation as National Facility managed by CSIRO until 2012.

Facilities: Mopra, NANTEN2.

REFERENCES

Bains, I., Wong, T., Cunningham, M. R. et al., 2006, MNRAS, 367, 1609

Batchelor R. A., Caswell J. L., Haynes R. F. et al. 1980, AuJPh, 33, 139

Becklin E. E., Frogel J. A., Neugebauer G. et al., 1973, ApJ, 182, L125

Breen, S. L., Ellingsen, S. P., Johnston-Hollitt, M. et al., 2007, MNRAS, 377, 491-506

Caswell J. L., Vaile R. A., Ellingsen S. P. et al., 1995, MNRAS, 272, 96

Caswell J. L., 1998, MNRAS, 297, 215

Csengeri, T., Urquhart, J. S., Schuller, F. et al., 2014, A&A, 565, 75

Figuerêdo, E., Blum, R. D., Damineli, A. et al., 2005, AJ, 129, 1523-1533

Fujiyoshi T., Smith C. H., Caswell J. L. et al., 2006, MNRAS, 368, 1843

Garden, R. P., Hayashi, M., Hasegawa, T. et al., 1991, ApJ, 374, 540

Glover, S. C. O., Clark, P. C., Micic, M., Molina, F., 2014, MNRAS, submitted, arXiv:1403.3530

Grave J. M. C., Kumar M. S. N., Ojha D. K. et al., 2014, A&A, 563, AA123

Ladd, N., Purcell, C., Wong, T. & Robertson, S. 2005, PASA, 22, 62

Lo, N., Cunningham, M., Bains, I. et al., 2007, MNRAS, 381, L30-L34

Lo, N., Cunningham, M. R., Jones, P. A. et al., 2009, MNRAS, 395, 1021

Lockman F. J., 1979, ApJ, 232, 761

Minier V., Tremblin, P., Hill, T. et al., 2013, A&A, 550, AA50

Mookerjea, B., Kramer, C., Nielbock, M., Nyman, L.-Å., 2004, A&A, 426, 119

Murphy, D. C., May, J., 1991, A&A, 247, 202-214

Netterfield, C. B., Ade, P. A. R., Bock, J. J., 2009, ApJ, 707, 1824

Offner, S. S. R., Bisbas, T. G., Bell, T. A., Viti, S., 2014, MNRAS, 440, 81

Oka, T., Yamamoto, S., Iwata, M. et al., 2001, ApJ, 558, 176

Roman-Lopes, A., Abraham, Z., Ortiz, R., & Rodriguez-Ardila, A. 2009, MNRAS, 394, 467

Shetty, R., Glover, S. C., Dullemond, C. P., Klessen, R. S., 2011, MNRAS, 412, 1686

Shimajiri, Y., Sakai, T., Tsukagoshi, T. et al., 2013, ApJL, 774, L20

Van der Tak, F.F.S., Black, J.H., Schier, F.L., Jansen, D.J., van Dishoeck, E.F., 2007, A&A, 468, 627

Wong, T., Ladd, E. F., Brisbin, D. et al., 2008, MNRAS, 386, 1069

Yamaguchi, N., Mizuno, N., Saito, H. et al., 1999, PASJ, 51, 775

This manuscript was prepared with the AAS LaTeX macros v5.2.